



HAL
open science

Prediction of turbulence generated by non-homogeneous grids for applications to experimental atmospheric boundary layer generation

Huret Thomas, Vassilicos Christos, Tanguy Geoffrey, Jacquin Laurent, Gallas Quentin

► **To cite this version:**

Huret Thomas, Vassilicos Christos, Tanguy Geoffrey, Jacquin Laurent, Gallas Quentin. Prediction of turbulence generated by non-homogeneous grids for applications to experimental atmospheric boundary layer generation. International Workshop on Physical Modeling of Flow and Dispersion Phenomena PHYSMOD 2022, Aug 2022, Prague, Czech Republic. hal-03784831

HAL Id: hal-03784831

<https://hal.science/hal-03784831>

Submitted on 23 Sep 2022

HAL is a multi-disciplinary open access archive for the deposit and dissemination of scientific research documents, whether they are published or not. The documents may come from teaching and research institutions in France or abroad, or from public or private research centers.

L'archive ouverte pluridisciplinaire **HAL**, est destinée au dépôt et à la diffusion de documents scientifiques de niveau recherche, publiés ou non, émanant des établissements d'enseignement et de recherche français ou étrangers, des laboratoires publics ou privés.



Prediction of turbulence generated by non-homogeneous grids for applications to experimental atmospheric boundary layer generation

HURET Thomas¹, VASSILICOS Christos¹, TANGUY Geoffrey¹, JACQUIN Laurent², GALLAS Quentin³

¹ Univ. Lille, CNRS, ONERA, Arts et Métiers Institute of Technology, Centrale Lille, UMR 9014 –LMFL – Laboratoire de Mécanique des Fluides de Lille –Kampé de Fériet, F-59000 Lille, France

² DAAA, ONERA, Université Paris-Saclay, F-92190 Meudon –France

³ ONERA–The French Aerospace Lab, 31410 Maucac, France

1. Introduction

1.1 The neutral Atmospheric Boundary Layer (ABL)

The wind tunnel configurations studied in this work are representative of neutral ABL over flat surfaces of homogeneous roughness, quantified by the “roughness length” h_0 . This quantity is defined through the mean velocity profile obtained in the Inertial SubLayer (ISL) of the ABL

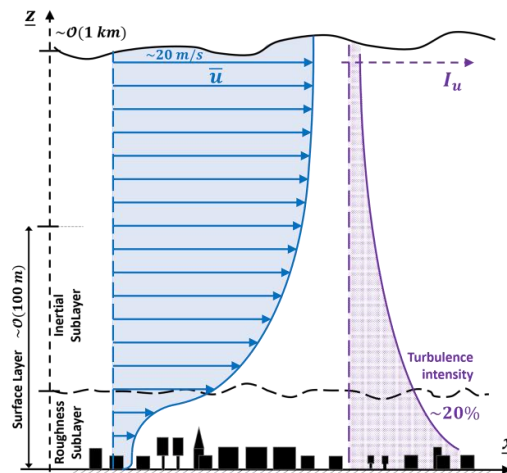


Figure 1: Schematic visualization of the neutral Atmospheric Boundary Layer. Based on [10][11].

The ISL is characterized by a logarithmic dependency with the altitude [10] (see Figure 1), as described by the equation:

$$\bar{u}(z) = \frac{u_*}{\kappa} \ln\left(\frac{z-d}{h_0}\right) \quad (1)$$

The friction velocity u_* is defined as $u_* := \sqrt{\frac{\tau_{friction \rightarrow wall}}{\rho}} \approx \sqrt{-\langle u'w' \rangle_{wall}}$ and $\kappa \sim 0.4$ is considered.

The generation of atmospheric boundary layer within short aeronautic wind tunnels requires to thicken artificially the otherwise naturally growing rough-wall boundary layer. Several attempts were made to achieve this boundary layer thickening with both passive or active devices [2]. The successful Counihan-type passive configurations [1,18] inspired Cook (1978) [3] who presented a

family of similar devices and suggested a general understanding of the behaviour of such passive devices, named as “Roughness-Barrier-Mixing device method” (RBM).

However, almost all past devices require a trial-and-error step in their design process, which must be reproduced for each new studied configuration (i.e. new roughness condition) and each new wind tunnel setup. This was observed by Cook (1978) [3] who undertook a parametric analysis on their devices to relate the effective roughness length and integral length scales to their geometric parameter (the height of the wall component).

1.2 Objectives

The present work aims at investigating Multiscale Inhomogeneous Grids (MIGs) as a new type of device for wind tunnel generation of ABL flows. Indeed, their design is expected to enable tailoring (without trial-and-error) both mean flow profile and turbulent intensity profiles, by taking advantage of tools developed initially for fractal grids studies. The next section presents the past work establishing ways to design a grid for a given mean flow profile. The last sections introduce the theoretical model for turbulence intensity predictions.

2. Multiscale Inhomogeneous Grids (MIGs) design

2.1 Multiscale Inhomogeneous Grids

Multiscale Inhomogeneous Grids [18] are composed of regular arrays of vertical bars within several horizontal levels of varying geometric properties (w_n, g_n, h_n , see Figure 3).

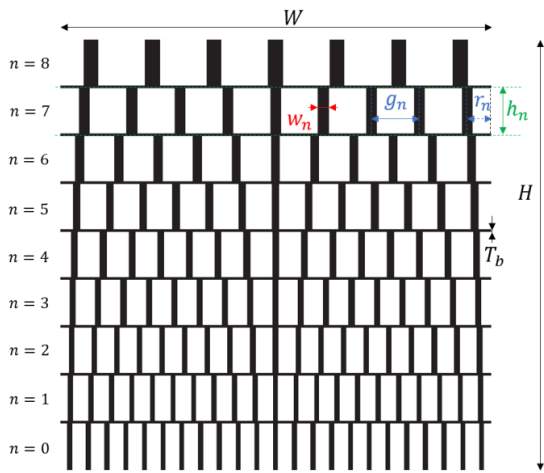


Figure 3: Several passive devices for the generation of a neutral ABL in wind tunnel

Notation	Definition
N	Number of layers
W	Width of the grid section
H	Height of the grid section
T_n	Width of the horizontal bars
d_n	Streamwise depth of the horizontal bars
h_n	Height of each layer (horizontal Bars center to center)
g_n	Distance between adjacent vertical bars (cent. to cent.)
r_n	Distance from the wall of the first vertical bar of the level
w_n	Width of vertical bars
d_n	Streamwise depth of vertical bars
c_n	Number of vertical bars
σ_n	Blockage ratio (solidity) of the layer

Table 1: Definition of the different geometric parameters of MIG grid.

2.2 Theoretical prediction of the mean flow profile

The MIGs are composed of multiple horizontal layers, each of them harbouring an array of vertical bars of the same width. Width and distance between two vertical bars are dependent of the grid level. The non-uniform local blockage ratio that is produced generates a non-uniform pressure jump between the two sides of the grid. This pressure jump, normalized as $K = (P_{0-} - P_{0+}) / \frac{1}{2} \rho u_0^2$ in the following, produces a non-uniform pressure field upstream and downstream, both of which

influencing the mean flow velocity. The grid geometry is therefore a way to convert the far upstream mean flow distribution $u^{-\infty}$ into a sheared mean flow far downstream $u^{+\infty}$ (see Figure 3).

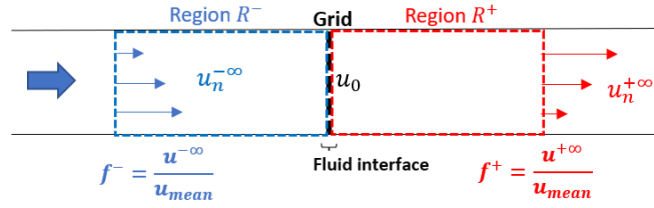


Figure 4: Schematic visualization of the regions of influence of the grid upstream and downstream within the wind tunnel. Inspired from [19]

Elder (1959) [22] and then by McCarthy (1964) [19] suggested an analytical formulation relating the far mean flows with the grid geometry.

McCarthy (1964) model

McCarthy (1964) [19] considered the far upstream flow to be perfectly homogeneous ($du^{-\infty} = 0$ and $u^{-\infty} = u_{mean}$) so that the problem consists in solving a non-linear Ordinary Differential Equation (ODE) on $u^{+\infty}$ as a function of $\chi = \sqrt{1 + K}$. This equation was solved analytically by approximating several integrals up to the second order (see [19]). The resulting relation is given in the first box of Figure (5) for a problem discretized over the N levels of the designed grid.

This non-linear coupled equation system is inverted by a Sequential Least Squares Programming (SLSQP) algorithm in order to find the $\{K_n\}_n$ distribution for a given objective function f_n^+ .

A numerical solving model

Another way to solve Equation (2) without asking for extra hypothesis on the upstream mean flow (or analytical approximations) consists in solving it numerically. For prescribed normalized upstream and downstream mean flow, Equation (2) can be rewritten as an ODE on χ as a function of the altitude z . The resulting equation is given in the second box of Figure (6)), where $G_+(\chi) = 1 + \frac{\chi^2 - 1}{1 + \frac{B}{\chi}}$;

$$G_-(\chi) = \frac{\frac{B}{\chi}(\chi^2 - 1)}{1 + \frac{B}{\chi}} - 1; \mathcal{M}(\chi) = \frac{B}{\chi^2} \frac{\chi^2 - 1}{1 + \frac{B}{\chi}}; \mathcal{L}(\chi) = \frac{B}{\chi^2} \frac{\chi^2 - 1}{(1 + \frac{B}{\chi})^2} + \frac{\chi}{1 + \frac{B}{\chi}}$$

The solution of this problem, numerically computed using a Runge-Kutta 4 (RK4) method, is then discretized over N grid levels. A dichotomy algorithm is used to find the initial condition corresponding to the prescribed mean obstruction over the full section.

2.3 Grid design algorithm

Using the mean flow tailoring tools described above, a grid design algorithm was implemented in two versions depending of the modelling choice. They can be visualized schematically in Figure (5) and Figure (6). Choice was made to arbitrarily fix the distance g_n between two adjacent bars and the height of each grid level, since they represent extra-degrees of freedom that will become useful only for generating prescribed turbulence profiles.

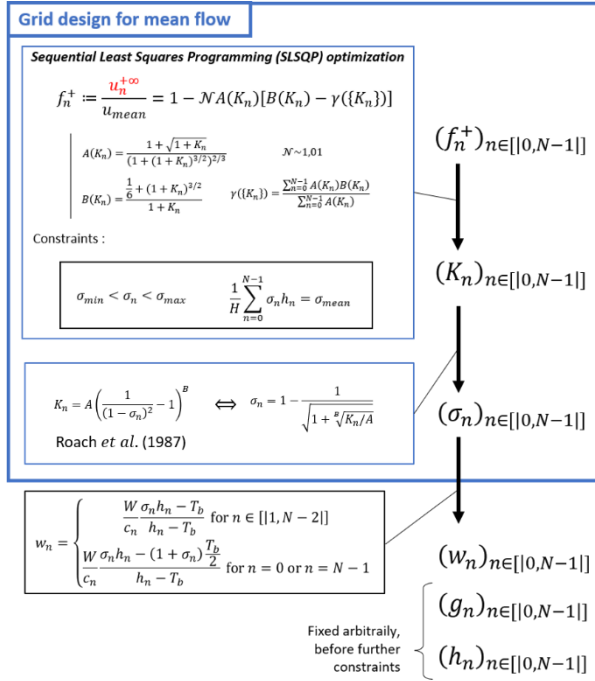


Figure 5: Schematic representation of the grid design algorithm using the McCarthy (1964) [19] model.

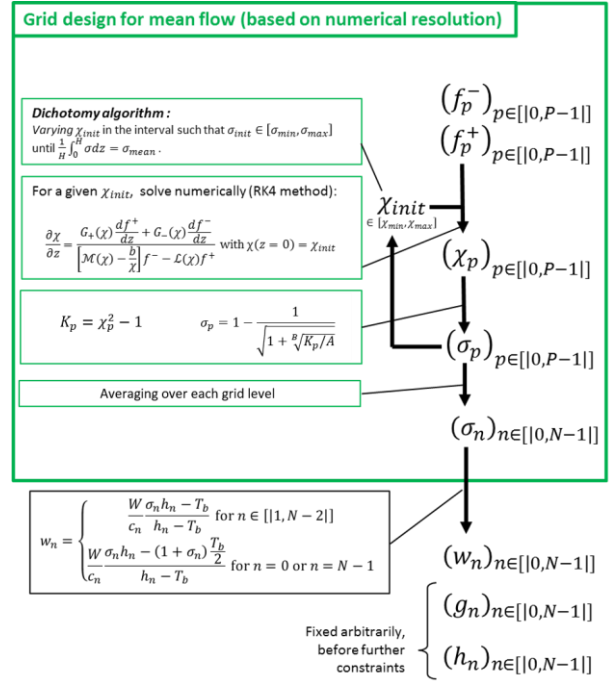


Figure 6: Schematic representation of the grid design algorithm solving Equation (2) numerically.

The design for grids dedicated to the generation of a logarithmic mean flow is fully characterized by two inputs parameters: the mean blockage ratio σ_{mean} (averaged over the full wind tunnel section area) and the non-dimensional roughness ratio h_0/H .

3. Experimental setup

3.1 Hot-wire Anemometry in SCL-PIV wind tunnel (ONERA Lille)

The SCL-PIV wind tunnel (ONERA Lille) is dedicated to boundary layer studies. The working section of $H \times W = 0.29 \text{ m} \times 0.30 \text{ m}$ enables an exploration by both Hot-Wire Anemometry (HWA) and Particle Image Velocimetry (PIV). The operational velocity range is between 10 m/s and 30 m/s . The current work presents HWA results obtained for a reference velocity of $U_{pitot} = 15 \text{ m/s}$ (global Reynolds number $Re = U_{pitot}H/\nu \sim 2.78 \times 10^5$).

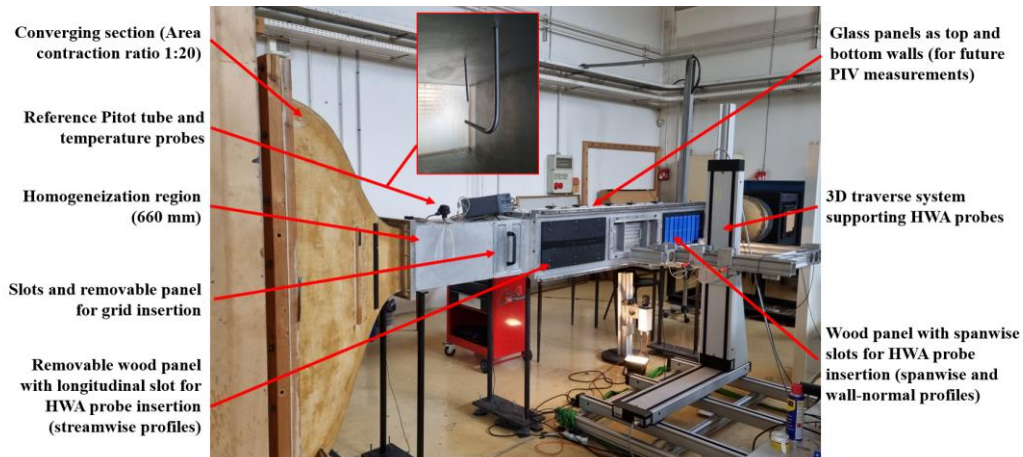


Figure 7: The SCL-PIV wind tunnel (ONERA Lille).

Two different Hot-Wire probes are considered: a single Hot-Wire (Dantec 55P15) probe with frequency response up to very high frequencies for spectral studies. It also enables to reach points close to the wall ; a X-cross Hot-Wires probe (Dantec 55R51) leading to two velocity components and Reynolds stress measurements. For every acquisition point of the present work, a signal of 30s is acquired at $f_{acq} = 100 \text{ kHz}$ (Analog low-pass filter at $f_{cutoff} = 30 \text{ kHz}$). The current work presents results measured across the “IIIT9-center” profile (wall normal profile) visible in red in Figure (9).

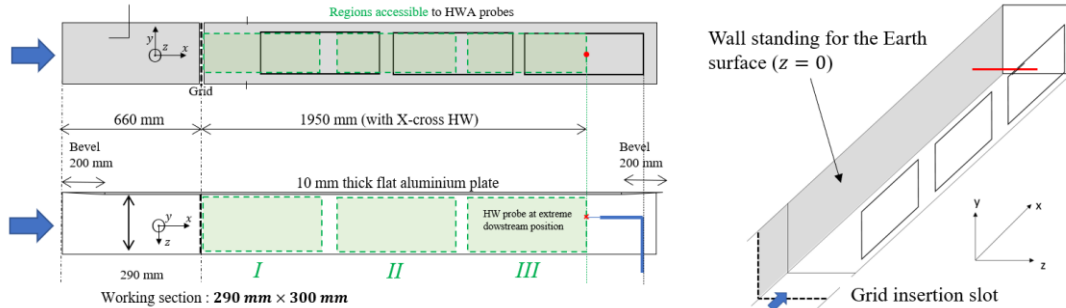


Figure 9: Schematic visualization of the wind tunnel working section. The studied profile is highlighted in red.

3.2 Roughness characterisation

In order to reproduce the surface layer of the ABL (see Figure (1)), the Jensen similarity criterium requires that the “roughness length” of the considered terrain must be represented at scale in the wind tunnel. By default, the wind tunnel is in a “smooth configuration” (flat aluminium plate with measured $h_0^{smooth} = 0.0025 \text{ mm}$ comparable to estimations from [12]). Adding LEGO® Baseboards on the flat plate leads to the “rough” configuration (with $h_0^{LEGO} = 0.13 \text{ mm}$, comparable with [1]).

3.3 Definition of the 6 grids

In the present work, six different grids were designed in order to fit within the SCL-PIV slot. The five first grids/obstacles are designed in order to generate the same logarithmic mean flow with artificial roughness $h_0^{objective} / H = 4.5 \times 10^{-4}$ (compatible with LEGO® Baseboard).

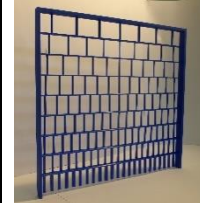

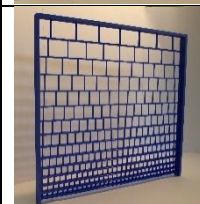
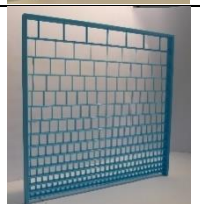
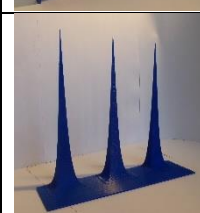
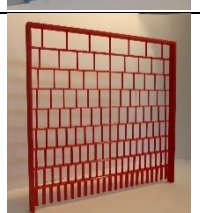
	<p>MIG-log-LEGO_N9 9 levels of same height. Designed with the McCarthy model (1964) [19].</p> <p>$h_0/H = 4.5 \times 10^{-4}$. $\sigma_{mean} = 0.2$ $\sigma_{max} = 0.389$</p>		<p>MIG-log-LEGO_N15 15 levels of same height. Designed with the McCarthy model (1964) [19].</p> <p>$h_0/H = 4.5 \times 10^{-4}$. $\sigma_{mean} = 0.2$ $\sigma_{max} = 0.442$</p>
	<p>MIGnh-log-LEGO_N15 15 levels of increasing height (power law of the altitude). Designed with the McCarthy model (1964) [19].</p> <p>$h_0/H = 4.5 \times 10^{-4}$. $\sigma_{mean} = 0.2$ $\sigma_{max} = 0.597$</p>		<p>MIGnh-rk4-log-LEGO_N15 15 levels of increasing height (power law of the altitude). Designed with the numerical solving (RK4) of Equation (2) [19].</p> <p>$h_0/H = 4.5 \times 10^{-4}$. $\sigma_{mean} = 0.2$ $\sigma_{max} = 0.630$</p>
	<p>MIGspires-log-LEGO_N500 500 levels. No horizontal bar. Only three vertical bars at each level, leading to three spires. Designed with the McCarthy model (1964) [19].</p> <p>$h_0/H = 4.5 \times 10^{-4}$. $\sigma_{mean} = 0.2$</p>		<p>MIG-log-1e-3_N9 9 levels of same height. Designed with the McCarthy model (1964) [19].</p> <p>$h_0/H = 10^{-3}$. $\sigma_{mean} = 0.2$ $\sigma_{max} = 0.413$</p>

Figure 12: Main characteristics of the 6 grids designed using the algorithm of the previous section. The grids are all 3D printed in PLA with a 100% fill. $H = 290 \text{ mm}$.

4. Experimental investigations

4.1 Grid-generated mean flow profiles

The measurements by X-cross hot-wire at the “IIIT9-Center” profile (see Section 3.1) downstream of the grid “MIGnh-rk4-log-LEGO_N15” is presented in Figure (13). Similar conclusions can be drawn for the other grids (to the exception of the “MIG-spires-log-LEGO_N500”).

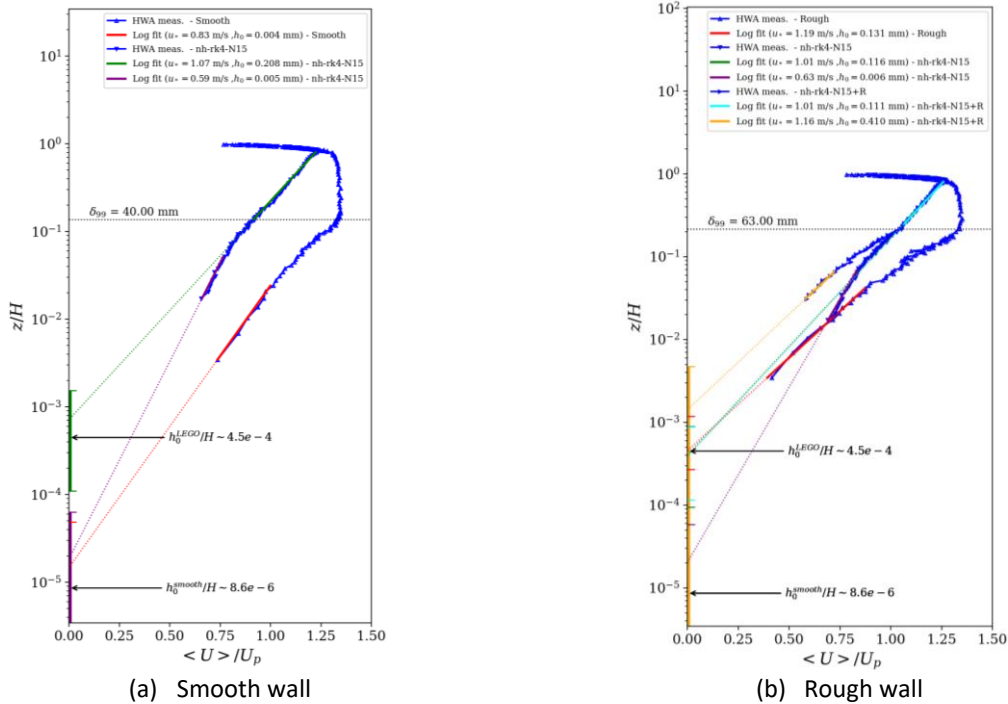


Figure 13: Mean longitudinal mean flow velocity profile measured at position $x = 1950 \text{ m}$ downstream of MIGnh-rk4-log-LEGO_N15.

In Figure (13), two different regions are visible: a wall-region of approximately the same height as the natural boundary layer growing in empty vein configuration, and a center vein region (roughly between $0.2H$ and $0.8H$). The profiles within these two regions are fitted by logarithmic laws in order to estimate their equivalent friction velocities and roughness lengths. The 95%-confidence intervals for the estimation of roughness length are presented as continuous lines on plots of Figure (13).

With the 6 different grids or obstacles designed using these models, the center vein region is shown to depend mainly on the grid characteristics, showing a good match with the expected mean velocity profiles.

However, the wall-region remain mainly influenced by the wall roughness. Surprisingly, an attempt to reach roughness similarity lead to larger discrepancies, except for the “spires” configuration which shows a very good match with the expected mean flow even within the wall region. This reveals that the geometric differences between grid and spires have a significant influence on the interaction with roughness. This is probably due to the larger vortex structures produced by spires, which enable a coupling of flow layers over a significant range of altitudes (as explained by Cook (1978) [3]). Downstream of passive grids, turbulent structures scale with the mesh size (e.g. [28,29]) and are probably too small to produce the same effect as spires.

4.3 Grid-generated turbulence intensity

The streamwise turbulence intensity measured at the location “IIIT9-Center” (see Section 3.1) corresponding to “MIG-nh-rk4-log-LEGO_N15” (d) and “MIG-spires-log-LEGO_N500” (e) are presented in Figure (15). Conclusions with the other grids are similar to the one with “MIG-nh-rk4-log-LEGO_N15”.

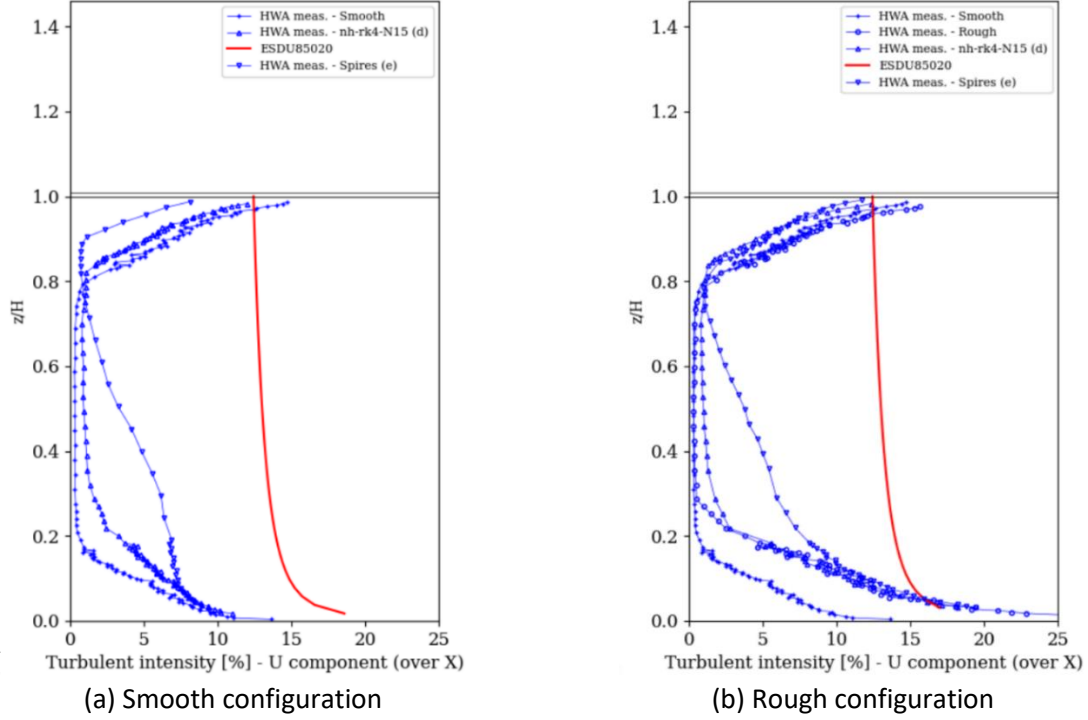


Figure 15: Streamwise turbulent intensity measured by HWA in SCL-PIV at the location of the “IIIT9-Center” profile. The profiles are compared to the ESDU85020 atmospheric model [27] adapted with the LEGO® Baseboard roughness length.

From Figure (15), the “Smooth configuration” presents a turbulence level too low compared to the atmospheric case even close to the wall. As expected, it improves close to the wall when roughness is added, even though no clear changes are visible in the center region. Contrary to “spires” which maintain high turbulence intensity far from the wall, the grid generated turbulence decay quickly to values smaller than 3%, in accordance with previous observations (Cook (1978) [3]).

5. Turbulence intensity model

5.1 Fractal grid-generated turbulence evolution

Previous studies focusing on the turbulence evolution downstream of fractal grids validated a scaling law (Equation (8)) relating turbulence intensity with the downstream distance (Gomez-Fernandez et al. 2012).

$$\frac{\sqrt{2k}}{\bar{u}} = \frac{1}{\beta} \sqrt{\frac{C_d w_n}{x_*^{peak}}} \mathbf{g} \left(\frac{x}{x_*^{peak}}, * \right) \quad (8)$$

Where $k = \frac{1}{2}\langle u'^2 + v'^2 + w'^2 \rangle$, $\beta \sim 2.88$ and C_d stands for the drag coefficient associated to one isolated grid bar. This scaling depends on the length scale x_*^{peak} describing the position of the maximum of turbulent intensity. It can be interpreted as a characteristic streamwise interaction distance between two adjacent planar wakes. It can be expressed as in Equation (9).

$$x_*^{peak} = \Gamma \frac{g_n^2}{\alpha C_d w_n}$$

Where $\Gamma \sim 0.21$ and $\alpha \sim 0.24$ are coefficients empirically deduced by Symes & Fink (1977) [] and Gomes-Fernandes et al (2012) [] respectively. The scaling of Equation (8) was experimentally validated for fractal and regular grids, as can be seen with the good collapse of several curves (for several grids) in Figure ().

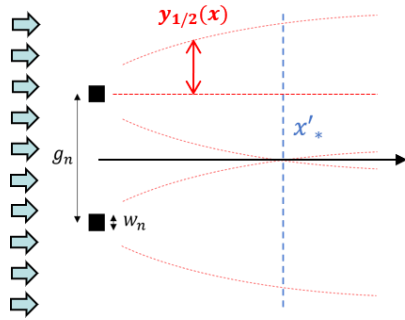


Figure (): Two interacting wakes. By definition, $y_{1/2}$ is the spanwise distance at which the velocity defect is half of its maximum value. From planar wake theory, $x'_* = g_n^2 / \alpha C_d w_n$ (Gomes-Fernandes et al. 2012)

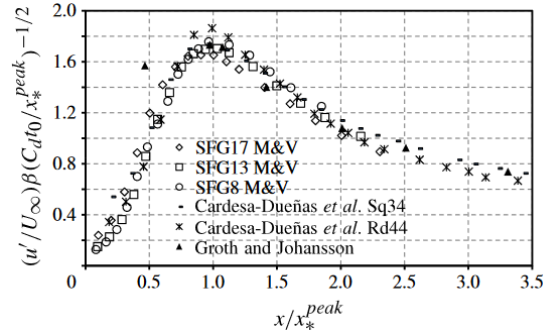


Figure (): Downstream evolution of normalized turbulence intensity for several fractal and regular grids. Extracted from Gomes-Fernandes et al. (2012).

However, Equation (8) was validated for flows in absence of mean shear. The next section is therefore describing an attempt to take into account the more complex set of parameters that is required to represent accurately atmospheric flows.

5.2 A theoretical attempt to take into account mean shear in turbulence prediction

The Turbulent Kinetic Energy (TKE) equation is written in its incompressible form as Equation ().

$$\begin{aligned} \bar{u} \frac{\partial k}{\partial x} = & \left. \begin{aligned} -\langle u'^2 \rangle \frac{\partial \bar{u}}{\partial x} & \quad -\langle u'v' \rangle \frac{\partial \bar{u}}{\partial y} & \quad -\langle u'w' \rangle \frac{\partial \bar{u}}{\partial z} \end{aligned} \right\} \mathcal{P} \\ & \left. \begin{aligned} -\frac{\partial}{\partial x} \langle u'q^2 \rangle & \quad -\frac{\partial}{\partial y} \langle v'q^2 \rangle & \quad -\frac{\partial}{\partial z} \langle w'q^2 \rangle \end{aligned} \right\} \mathcal{T} \\ & \left. \begin{aligned} -\frac{\partial}{\partial x} \langle u'p' \rangle & \quad -\frac{\partial}{\partial y} \langle v'p' \rangle & \quad -\frac{\partial}{\partial z} \langle w'p' \rangle \end{aligned} \right\} \mathcal{II} \\ & \left. -\nu \left\langle \frac{\partial u_i}{\partial x_1} \frac{\partial u_i}{\partial x_1} \right\rangle \right\} \mathcal{E} \end{aligned} \quad (5)$$

With $q^2 = u'^2 + v'^2 + w'^2$ and p' the pressure fluctuating component. \mathcal{P} refers to production terms of turbulence, \mathcal{T} refers to triple-correlation transport terms, \mathcal{II} refers to pressure-velocity transport terms and \mathcal{E} refers to turbulent rate of dissipation.

Let us now consider the following assumptions in the region of decay of turbulence:

- I. Spanwise homogeneity of the flow $\frac{\partial \bar{u}}{\partial y} = 0$
- II. Lateral velocity fluctuations are proportional to the streamwise velocity fluctuation (an isotropy hypothesis): $\sqrt{\langle v'^2 \rangle} = \xi_2 \sqrt{\langle u'^2 \rangle}$ and $\sqrt{\langle w'^2 \rangle} = \xi_3 \sqrt{\langle u'^2 \rangle}$
- III. Streamwise triple-correlation transport can be neglected. $\left| \frac{\partial}{\partial x} \langle u'^3 \rangle \right| \ll \bar{u} \left| \frac{\partial}{\partial x} \langle u'^2 \rangle \right|$ (Harris et al. 1977), such that : $\frac{\partial}{\partial x} \langle u' \frac{q^2}{2} \rangle = \frac{1+\xi_2^2+\xi_3^2}{2} \frac{\partial \langle u'^3 \rangle}{\partial x} \ll \frac{1+\xi_2^2+\xi_3^2}{2} \bar{u} \frac{\partial \langle u'^2 \rangle}{\partial x} = \bar{u} \frac{\partial k}{\partial x}$
- IV. Remaining turbulent transport terms are proportional to the dissipation rate (following Valente & Vassilicos 2011): $\frac{\partial}{\partial y} \langle v' \frac{q^2}{2} \rangle = \chi_2(\mathbf{y}, \mathbf{z}) \mathcal{E}$ and $\frac{\partial}{\partial z} \langle w' \frac{q^2}{2} \rangle = \chi_3(\mathbf{y}, \mathbf{z}) \mathcal{E}$
- V. Turbulent pressure-velocity terms are proportional to the dissipation rate (following Valente & Vassilicos 2011): $\Pi = \chi_{\Pi}(\mathbf{y}, \mathbf{z}) \mathcal{E}$

These assumptions, in association with the formulation $\mathcal{E} = C_{\varepsilon}(x) \frac{k^{\frac{3}{2}}}{L_{uu,x}(x)}$ (Vassilicos 2015 []) led to transform the equation () into:

$$\frac{\partial k}{\partial x} = - \frac{S_1 + \rho_* S_3}{\bar{u} \left[\frac{1 + \xi_2^2 + \xi_3^2}{2} \right]} k - \frac{\chi C_{\varepsilon}}{\bar{u} L_{uu,x}} k^{3/2}$$

With $S_1 = \frac{\partial \bar{u}}{\partial x}$, $S_3 = \frac{\partial \bar{u}}{\partial z}$, $\rho_* = \xi_3 \frac{\langle uw' \rangle}{\sqrt{u'^2} \sqrt{w'^2}}$, $\chi = 1 + \chi_2 + \chi_3 + \chi_{\Pi}$ and $L_{uu,x}$ is the streamwise integral length scale.

References

- [1] J. Counihan, "An improved method of simulating an atmospheric boundary layer in a wind tunnel," *Atmospheric Environment* (1967), vol. 3, no. 2 : 197–200, 1969.
- [2] J. C. R. Hunt and H. Fernholz, "Wind-tunnel simulation of the atmospheric boundary layer: a report on Euromech 50," *Journal of Fluid Mechanics*, vol. 70, no. 3, pp. 543–559, Aug. 1975.
- [3] N. J. Cook, "Wind-tunnel simulation of the adiabatic atmospheric boundary layer by roughness, barrier and mixing-device methods," *Journal of Wind Engineering and Industrial Aerodynamics*, vol. 3, no. 2, pp. 157–176, Jan. 1978.
- [4] H. P. A. H. Irwin, "The design of spires for wind simulation," *Journal of Wind Engineering and Industrial Aerodynamics*, vol. 7, no. 3, pp. 361–366, May 1981.
- [5] R. J. Hearst and B. Ganapathisubramani, "Tailoring incoming shear and turbulence profiles for lab-scale wind turbines," *Wind Energy*, vol. 20, no. 12, pp. 2021–2035, Dec. 2017.
- [6] J. E. Cermak, "Laboratory Simulation of the Atmospheric Boundary Layer," *AIAA Journal*, vol. 9, no. 9, pp. 1746–1754, Sep. 1971.
- [7] R. Avissar, M. D. Moran, G. Wu, R. N. Meroney, and R. A. Pielke, "Operating ranges of mesoscale numerical models and meteorological wind tunnels for the simulation of sea and land breezes," *Boundary-Layer Meteorol*, vol. 50, no. 1, pp. 227–275, Mar. 1990.
- [8] J. Armit and J. Counihan, "The simulation of the atmospheric boundary layer in a wind tunnel," *Atmospheric Environment* (1967), vol. 2, no. 1, pp. 49–71, Jan. 1968.
- [9] M. Jensen and N. Franck, "Model-scale tests in turbulent wind," 1963.
- [10] A. S. Monin and A. M. Obukhov, "Basic laws of turbulent mixing in the surface layer of the atmosphere," *Tr. Akad. Nauk. SSSR Geophys. Inst.*, vol. 24, no. 151, pp. 163–187, 1954.

- [11] J. C. Kaimal and J. J. Finnigan, *Atmospheric Boundary Layer Flows: Their Structure and Measurement*. Oxford, New York: Oxford University Press, 1994.
- [12] M. R. Raupach, R. A. Antonia, and S. Rajagopalan, "Rough-Wall Turbulent Boundary Layers," *Applied Mechanics Reviews*, vol. 44, no. 1, pp. 1–25, Jan. 1991.
- [13] J. Wieringa, "Updating the Davenport roughness classification," *Journal of Wind Engineering and Industrial Aerodynamics*, vol. 41, no. 1, pp. 357–368, Oct. 1992.
- [14] A. Davenport, C. Grimmond, T. Oke, and J. Wieringa, "Estimating the roughness of cities and sheltered country," *15th conference on probability and statistics in the atmospheric sciences/12th conference on applied climatology, Asheville, NC, American Meteorological Society*, pp. 96–99, Jan. 2000.
- [15] A. G. Davenport and N. Isyumov, "The application of a the boundary layer wind tunnel to the prediction of wind loading," 1967.
- [16] J. Counihan, "Further measurements in a simulated atmospheric boundary layer," *Atmospheric Environment (1967)*, vol. 4, no. 3, pp. 259–275, May 1970.
- [17] H. P. A. H. Irwin, "Design and use of spires for natural wind simulation," *Laboratory Technical Report (National Research Council of Canada. National Aeronautical Establishment. Low Speed Aerodynamics Laboratory)*, p. 65 p., Aug. 1979.
- [18] S. Zheng, P. J. K. Bruce, J. M. R. Graham, and J. C. Vassilicos, "Weakly sheared turbulent flows generated by multiscale inhomogeneous grids," *Journal of Fluid Mechanics*, vol. 848, pp. 788–820, Aug. 2018
- [19] J. H. McCarthy, "Steady flow past non-uniform wire grids," *Journal of Fluid Mechanics*, vol. 19, no. 4, pp. 491–512, Aug. 1964.
- [20] G. I. Taylor, G. K. Batchelor, H. L. Dryden, and G. B. Schubauer, "THE EFFECT OF WIRE GAUZE ON SMALL DISTURBANCES IN A UNIFORM STREAM," *Q J Mechanics Appl Math*, vol. 2, no. 1, pp. 1–29, Jan. 1949
- [21] P. R. Owen and H. K. Zienkiewicz, "The production of uniform shear flow in a wind tunnel," *Journal of Fluid Mechanics*, vol. 2, no. 6, pp. 521–531, Aug. 1957.
- [22] J. W. Elder, "Steady flow through non-uniform gauzes of arbitrary shape," *Journal of Fluid Mechanics*, vol. 5, no. 3, pp. 355–368, Apr. 1959.
- [23] U. Karnik and S. Tavoularis, "Generation and manipulation of uniform shear with the use of screens," *Experiments in Fluids*, vol. 5, no. 4, pp. 247–254, Jul. 1987.
- [24] K. E. G. Wieghardt, "On the Resistance of Screens," *Aeronautical Quarterly*, vol. 4, no. 2, pp. 186–192, Aug. 1953.
- [25] W. G. Cornell, "Losses of flow normal to plane screens," *Trans. ASME*, vol. 80, no. 4, pp. 791–799, 1958.
- [26] P. E. Roach, "The generation of nearly isotropic turbulence by means of grids," *International Journal of Heat and Fluid Flow*, vol. 8, no. 2, pp. 82–92, Jun. 1987.
- [27] ESDU 85020, "Characteristics of atmospheric turbulence near the ground - Part II: singlepoint data for strong winds (neutral atmosphere)." Engineering Sciences Data Unit, 1985.
- [28] P. C. Valente and J. C. Vassilicos, "The decay of turbulence generated by a class of multiscale grids," *Journal of Fluid Mechanics*, vol. 687, pp. 300–340, Nov. 2011.
- [29] J. Nedić and S. Tavoularis, "Energy dissipation scaling in uniformly sheared turbulence," *Phys. Rev. E*, vol. 93, no. 3, p. 033-115, Mar. 2016.